Monthly Notices
of the
ROYAL ASTRONOMICAL SOCIETY

MNRAS **505,** 4141–4150 (2021)
Advance Access publication 2021 May 4

https://doi.org/10.1093/mnras/stab1255

# Linking computational models to follow the evolution of heated coronal plasma

J. Reid [1]★ P. J. Cargill,[1,2] C. D. Johnston [1,3,4] and A. W. Hood [1]

[1] *School of Mathematics and Statistics, University of St Andrews, St Andrews, Fife KY16 9SS, UK*
[2] *Space and Atmospheric Physics, The Blackett Laboratory, Imperial College, London SW7 2BW, UK*
[3] *Department of Physics and Astronomy, George Mason University, Fairfax, VA 22030, USA*
[4] *NASA Goddard Space Flight Center, Greenbelt, MD 20771, USA*

Accepted 2021 April 27. Received 2021 April 27; in original form 2021 February 23

## ABSTRACT

A 'proof of principle' is presented, whereby the Ohmic and viscous heating determined by a three-dimensional (3D) MHD model of a coronal avalanche are used as the coronal heating input for a series of field-aligned, one-dimensional (1D) hydrodynamic models. Three-dimensional coronal MHD models require large computational resources. For current numerical parameters, it is difficult to model both the magnetic field evolution and the energy transport along field lines for coronal temperatures much hotter than 1 MK, because of severe constraints on the time step from parallel thermal conduction. Using the 3D MHD heating derived from a simulation and evaluated on a single field line, the 1D models give coronal temperatures of 1 MK and densities $10^{14}$–$10^{15}$ m$^{-3}$ for a coronal loop length of 80 Mm. While the temperatures and densities vary smoothly along the field lines, the heating function leads to strong asymmetries in the plasma flows. The magnitudes of the velocities in the 1D model are comparable with those seen in 3D reconnection jets in our earlier work. Advantages and drawbacks of this approach for coronal modelling are discussed.

**Key words:** MHD – methods: numerical – Sun: corona – Sun: magnetic fields.

## 1 INTRODUCTION

Multidimensional magnetohydrodynamic (MHD) computational models now play an important role in understanding the storage and release of energy in the solar corona (Reale 2014; Pontin & Hornig 2020). Increasingly complex physics can be included in such models, including, for example, radiative transfer and partial ionization in the chromosphere, as well as anisotropic thermal conduction, energy particle transport, and optically thin radiation in the corona. Examples include the Bifrost (Gudiksen et al. 2011), Pluto (Orlando et al. 2008), *Lare3d* (Botha, Arber & Hood 2011), and Pencil (Bingert & Peter 2011) codes. Additional numerical packages can generate synthetic 'observables', such as emission line profiles and emission measure distributions (e.g. Van Doorsselaere et al. 2016). However, several issues limit the utility of such models, especially the needs to ensure numerical stability and to distinguish between the various physical timescales.

In MHD models of low-$\beta$ plasmas that do not consider energy transport, the time step must satisfy:

$$\Delta t_{\rm MHD} < C_{\rm MHD} \min\left(\frac{|\Delta \boldsymbol{x}|}{|\boldsymbol{v}_A| + |\boldsymbol{v}|}\right), \tag{1}$$

in order to ensure numerical stability. Here, $C_{\rm MHD}$ is a Courant number, of the order of 0.25–0.5; $\boldsymbol{v}_A$ the Alfvén velocity; $\boldsymbol{v}$ the plasma velocity; and $\boldsymbol{\Delta x}$ the vector of grid spacing in each coordinate direction. On the right-hand side, the minimum is taken over the entire grid, in order to determine $\Delta t_{\rm MHD}$ globally. For an MHD simulation with a grid spacing of 100 km and an Alfvén speed of 2000 km s$^{-1}$, $\Delta t_{\rm MHD} \approx 0.02$ s.

When transport of energy is included, the major computational limitation is associated with thermal conduction along the magnetic field, which has a time step restriction:

$$\Delta t_c < \frac{1}{2} \min\left(\frac{3 n k_B \Delta s^2}{\kappa_0 T^{5/2}}\right), \tag{2}$$

where, again, the minimum value needs to be determined over the entire numerical grid and the coordinate $s$ lies parallel to the magnetic field. For a corona with $\Delta s = 100$ km, a density of $2 \times 10^{15}$ m$^{-3}$, and a temperature of 2 MK, $\Delta t_c \approx 7.5 \times 10^{-3}$ s. With techniques for addressing thermal conduction, such as super-time-stepping (implemented by Johnston et al. 2017a), $\Delta t_{\rm MHD}$ and $\Delta t_c$ contribute roughly equally to the time step restriction required for numerical stability. As a rule of thumb, a grid having $|\boldsymbol{\Delta x}| = \Delta s = 100$ km can model accurately coronal temperatures of the order of 1 MK (Bradshaw & Cargill 2013; Johnston et al. 2017a, 2020) and a number of contemporary MHD models that incorporate energy transport (such as those of Dahlburg et al. 2016, 2018) satisfy this criterion.

However, this is a 'best case' scenario. For temperatures typical of impulsively heated coronal plasmas, such as arise in nanoflares, microflares, and flares, $\Delta t_c$ decreases considerably. Exacerbating this is the need for very fine grids in order to model correctly thermal conduction between the corona and the chromosphere in the transition region (TR). The required resolution scales approximately with

★ E-mail: jr93@st-andrews.ac.uk

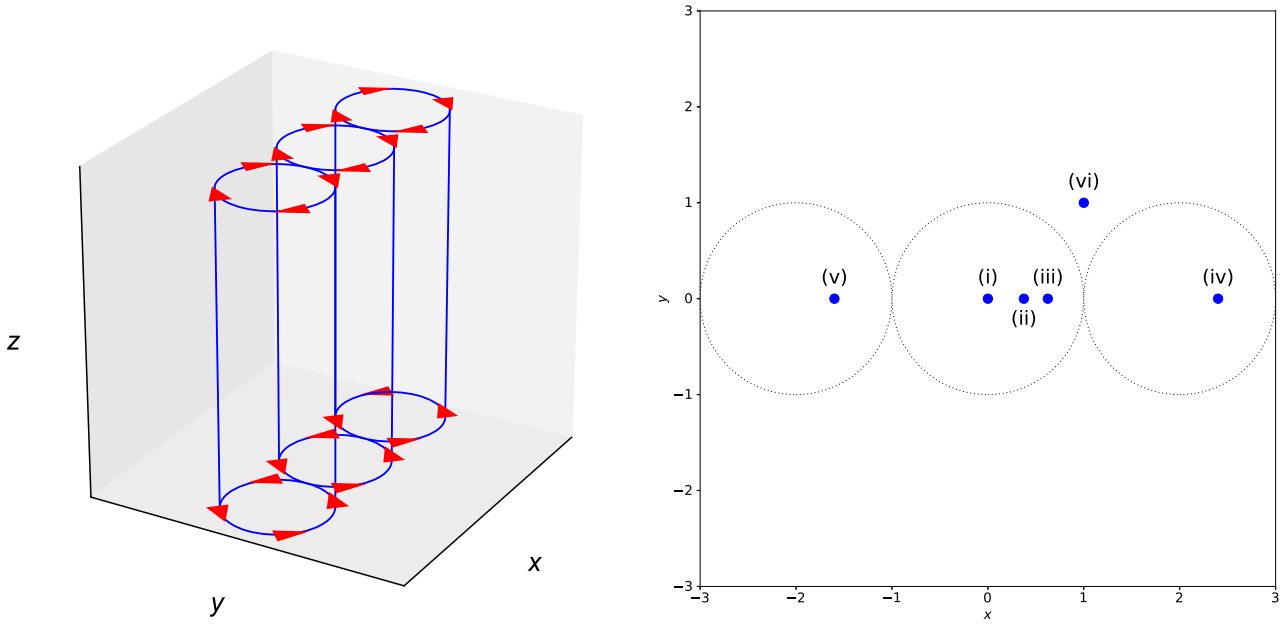


(a) Arrangement of threads. (b) Starting points of field lines.

**Figure 1.** (a) Arrangement of constituent strands within the loop of the 3D model (as in Reid et al. 2018). (b) Radii of the prescribed twisting motions on the photospheric planes, and, within those, the starting points (at $t = 0$, on the bottom boundary in the 3D simulation) for the field lines integrated and analysed (from Reid et al. 2020). The Roman numerals labelling each field line will be used throughout the paper.

$T^3$, so, for flaring plasmas (10 MK), $\Delta s$ can be of the order of tens of metres, leading to a reduction in $\Delta t_c$ by a factor of $10^6$ for a fixed grid. In the absence of this essential, high numerical resolution, the coronal density will be underestimated both for impulsive (Bradshaw & Cargill 2013) and for steady heating (Johnston et al. 2019), leading, in turn, to the construction of misleading coronal 'observables'.

An adaptive grid can mitigate this problem, but its implementation in multidimensional MHD is non-trivial, especially as there are other regions that may require high resolution, such as current sheets. Thus, the overhead cost on a three-dimensional (hereafter, 3D) MHD simulation of ensuring both numerical stability *and* adequate resolution of temperature gradients can be considerable.

In the long run, as computational power increases, it is likely that it will be feasible to achieve adequate resolution of the transition region within the framework of large-scale 3D MHD. However, in the meantime, there is value in examining alternative methods of modelling the coronal response to the release of energy in 3D models. This paper presents one such approach, which permits the fast and accurate calculation of coronal temperature and density. A 3D MHD code that does *not* model field-aligned thermal conduction and optically thin radiation can be used to determine the plasma heating along any given field line as a function of time and space. This heating can then be used as input for a one-dimensional (hereafter, 1D), field-aligned hydrodynamic model, which *does* include thermal conduction and optically thin radiation. We also use the new 'Transition Region using Adaptive Conduction' method (TRAC; Johnston & Bradshaw 2019; Johnston et al. 2020) in order to ensure rapid computation, although we note here that the TRAC method is not a universal panacea to the problems of 3D coronal MHD. We return to this aspect in the discussion. In addition to giving accurate coronal quantities, such an approach permits us to identify aspects of coronal behaviour, such as density and field-aligned flows arising from MHD effects, as opposed to being the result of the field-aligned evolution.

This paper presents a simple 'proof of principle' for such a method. Section 2 outlines our approach. Section 3 presents the results and their interpretation, and Section 4 discusses further the advantages and limitations of the method.

## 2 METHOD

The details of the coronal models and the methods used are presented by Reid et al. (2020) for 3D MHD, and by Johnston et al. (2020) for 1D hydrodynamic, simulations; only a brief summary is given here. The 3D coronal model is based on the three-strand avalanche model of Reid et al. (2018) and Reid (2020), sketched in Fig. 1(a).[1] Three initially cylindrical strands within a loop lie parallel to each other, and are attached to the photosphere at both ends. Motions at the photosphere twist these strands, the central one being twisted faster than the outer two. The twisted strands are surrounded by a region of straight magnetic field. The central strand undergoes a kink instability, which subsequently engulfs the outer two loops, leading to an avalanche. A bursty energy release results, and spreads throughout the domain.

### 2.1 MHD solution and determination of heating profile

The 3D MHD equations are solved using the *Lare3d* code (Arber et al. 2001).[2] A resistivity that switches on when the current exceeds a threshold permits magnetic reconnection to occur. Shocks are captured using a viscosity whose form and implications are

[1] We follow Klimchuk (2015) in using the word *strand* to denote a (possibly observable) magnetic sub-structure within a larger, organized magnetic field, such as a coronal loop.

[2] Further information is provided by Arber (2018) and, particularly as regards the viscosities, by Reid et al. (2020). Here, *Lare3d* v. 3.1.2 is used.

more fully discussed by Reid et al. (2020) and Reid (2020). The energy balance equation ignores thermal conduction and optically thin radiation. While *Lare3d* solves a set of dimensionless MHD equations, physical values of quantities are used for the purposes of calculating the plasma response. Using $512^2 \times 2048$ computational cells, in a Cartesian geometry as shown in Fig. 1(a), the simulated domain extends 27 Mm in each of the $x$- and $y$-directions, and 90 Mm in the $z$-direction, along the axis of the twisted strands. This implies a grid size of the order of 52 km in the $x$- and $y$-directions, and 44 km in the $z$-direction. The initial, uniform magnetic field is taken to have strength 10 G, giving an initial reference Alfvén speed of 690 km s$^{-1}$, for a number density of $10^{15}$ m$^{-3}$, leading to an Alfvén travel time of 6.52 s. Finally, the radius of each strand is 4.5 Mm. Since our previous work was presented exclusively in dimensionless units, we are now able to use the approach and analysis from Paper 2, with a simple rescaling of the MHD output as the input for the hydrodynamic modelling.

Both footpoints of each of the left-hand, central, and right-hand strands are rotated in the same sense, with maximum azimuthal velocities equal to 1, 2.5, and 1 per cent of the Alfvén speed, respectively, thereby inducing twist in the coronal magnetic field. As is common in 3D MHD simulations, the velocities are faster than in the real photosphere and so imply artificially compressed driving timescales.[3] This is necessary in order to separate the timescales defined by the Alfvén wave travel time, by numerical diffusion (from finite resolution), and by the driving (Bowness, Hood & Parnell 2013). The third of these must lie between the first and the second, and this is achieved for the above values.

The currents and mass motions arising in the avalanche are dissipated by the specific resistivity and the viscosities, both shock and background; this then enables us to determine a heating function with dependence on space and time. Across the 3D volume, the heating is found to be localized and temporally impulsive, but without any distinct preference in spatial distribution, as is related by Reid et al. (2020) (in particular, figs. 4, 7, and 11 thereof).

### 2.2 One-dimensional model

The field-aligned plasma evolution is followed with a 1D, Lagrangian remap code (*Lare1d*; Johnston 2018), which solves the non-linear hydrodynamic equations in a field-aligned geometry, including gravity; parallel Spitzer thermal conduction, of the form $\kappa_{\parallel} = \kappa_0 T^{5/2}$, where $\kappa_0 = 8.12 \times 10^{-12}$ J m$^{-1}$ K$^{-\frac{7}{2}}$ s$^{-1}$; optically thin radiation; and an imposed heating term. The radiative loss function of Klimchuk, Patsourakos & Cargill (2008) is used.

*Lare1d* includes a model chromosphere at both footpoints of a loop, and so makes no inherent assumption about symmetry about the loop apex, as is sometimes done. This model chromosphere acts as a mass reservoir, with the chromospheric base sufficiently deep that it is isolated from the coronal evolution. Following Johnston et al. (2017a), this chromosphere has a constant initial temperature of $10^4$ K, and gravitationally stratified density. Radiation is tapered from its coronal value as temperature decreases, following the formalism of Klimchuk et al. (2008).

[3]Models that do achieve driving speeds at the photospheric boundaries of the order of 1 km s$^{-1}$, as are observed, must compromise on other aspects, such as a very high density (as do Knizhnik et al. 2020) or greatly reduced physics, through, for example, incompressibility or weak perturbations (e.g. van Ballejooijen et al. 2011; Goldstraw et al. 2018). In simpler terms, this can be expressed as there being 'no such thing as a free lunch'.

Further, the cross-sectional area of the loops is constant. While localized deviations from this arise in the MHD simulations, they are small enough ($< 10$ per cent) to be of little consequence (for a further discussion of loops with non-uniform areas, Cargill et al., in preparation).

While, in principle, *Lare1d* could suffer from the usual limitations of a hydrodynamic model, namely a very short time step caused by the required resolution in the transition region (discussed in Section 1), an important modification (the TRAC method), developed by Johnston & Bradshaw (2019) and Johnston et al. (2020), removes this problem. Following earlier work of Lionello, Linker & Mikic (2009) and Mikić et al. (2013), the coefficient $\kappa_{\parallel}$ of thermal conduction is modified in the transition region, such that the gradients in temperature are spread over a larger number of computational cells. Far larger computational cells, and similarly longer time steps, can then be used. Further, by modifying optically thin losses, the radiative losses integrated across the region are the same when applying TRAC as when resolving fully the original Spitzer formulation for conduction. *Lare1d* here assumes a computational domain of 500 fixed, uniformly spaced computational cells. While this gives a coarser grid than used in the MHD model,[4] the use of the TRAC model means that all temperature gradients are fully resolved. TRAC has been tested and documented elsewhere (Johnston et al. 2020).

### 2.3 Coupling the methods

The 1D simulations require a prescribed heating function denoted $Q(s, t)$ (where $s$ is the distance along the chosen field line and $Q$ has units J m$^{-3}$ s$^{-1}$). We have selected six among a sample of field lines starting on the lower $z$-plane, with their initial locations shown in Fig. 1(b) and labelled (i)–(vi). These starting points of the field lines are advanced in time on this plane, according to the imposed rotational motions. The field lines are traced using a fourth/fifth-order Runge–Kutta–Fehlberg scheme, as implemented by Williams (2018). At each point along each field line, the local viscous heating and resistive heating are calculated by interpolation from the MHD grid. This determines $Q(s, t)$; we emphasize that the magnitude and temporal dependence of $Q$ from the MHD model are used in the 1D model. One complication of this simple approach is that the lengths of the field lines in the MHD model change as the avalanche evolves; this cannot be accounted for in the hydrodynamic model along a field line of fixed length. This is part of the interpolation from three dimensions to one. We have calculated the lengths of field lines in the MHD model as functions of time, and find that the change from the initial length of the straight field lines never exceeds 25 per cent. The issue of connectivity of field lines is discussed further in Section 4.

In the 1D model, a range of initial conditions have been used, and are further discussed in Appendix A. A uniform heating is imposed in order to attain the required initial coronal temperature, which ranges from $10^4$ to $2 \times 10^6$ K. The initial loop thus has a stratified atmosphere, with the model chromosphere at each footpoint, and a total length of 90 Mm (as in the MHD simulation). Of this, 10 Mm is in the two chromospheres, so that the coronal length of the initial loop is now 80 Mm. As the time-dependent simulation commences, this initial heating is switched off, and replaced with the heating functions determined from the MHD simulation. The aim of this procedure is to demonstrate that the heating from the 3D MHD model can sustain a loop with temperature and density characteristic of the observed corona.

[4]Compared with the MHD model's $\Delta z \sim \mathcal{O}$ (43.9 km), the TRAC model has $\Delta z \sim \mathcal{O}$ (180 km).

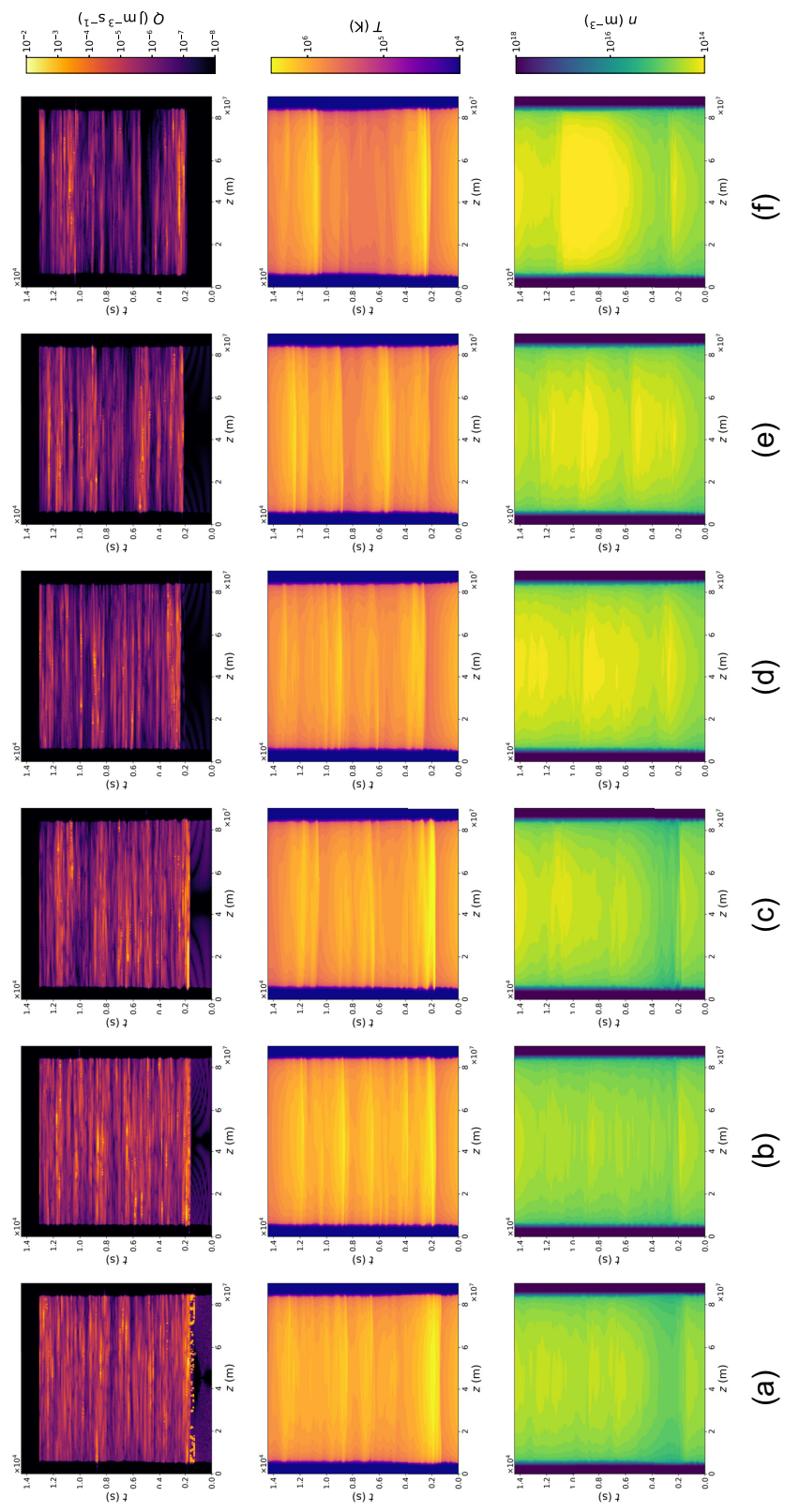


**Figure 2.** Heating function, $Q(s, t)$, taken from the 3D MHD model and inserted into the 1D model (upper row), and temperature (middle row) and number density (lower row) from the latter model, for the six field lines (i)–(vi), labelled as sub-panels (a)–(f). Time increases in the vertical direction, and the position along the field line along the horizontal axis, with the loop apex at the mid-point. The contours are drawn according to the respective scales shown in the colour tables. Regions in the contours of heating with a white space show heating below the minimum level on the colour bar. The white regions near the footpoints are the immediate consequence of the re-scaling of heating by the TRAC method (as described by Johnston et al. 2020).

## 3 RESULTS

Fig. 2 summarizes the results for the six field lines. The six columns show, from left to right, the field lines (i)–(vi) identified in Fig. 1(b). The top row shows the coronal heating profile $Q(s, t)$ for each field line chosen in the 3D model and used as input to the 1D model. The vertical axes show time, the horizontal axes distance along the field lines, and the colours the magnitudes of heating according to the colour table. Similarly, the middle and lowest rows show the temperature and density obtained from the hydrodynamic models as functions of space and time. The white bands on the left and right of the heating function correspond to the chromosphere, and are excluded in order to provide an accessible colour table. The heating in these regions is also small for two reasons. The analysis of Reid et al. (2020) indicated that heating near the footpoints was small, and the TRAC method also reduces the heating at low temperatures in order to conserve the integrated heating across the TR (Johnston et al. 2020).

The two columns of Fig. 3 show the average heating and coronal averages of the temperature, density, and parallel velocity as functions of time for field lines (ii), on the left, and (v), on the right. For the coronal averages, the mean is taken along the central 50 per cent of the field line. The blue curves in the temperature and density plots are the 1D solutions, the red and green curves are discussed below. The right column of Fig. 4 shows the behaviour of the parallel velocity as a function of space and time for field lines (ii) and (v) in the upper and lower rows, in the same format as in Fig. 2. Red and blue denote, respectively, flows parallel and anti-parallel to the field, with the magnetic field pointing in the positive $s$-direction. This colour coding should not be confused with the usual terminology for Doppler shifts. The plots in the left column of Fig. 4 are discussed below.

This simulation has an initial coronal temperature of 1.2 MK and coronal density of $4 \times 10^{14}$ m$^{-3}$; early evolution of $T$ and $n$ on all the field lines reflects the cooling of this plasma by thermal conduction, in the absence of sufficient heating. The declining density reflects the relatively large ratio $L/\Lambda$, where $\Lambda$ is the scale height, and is also evident in the early draining seen in the right column of Fig. 4. Field lines (i), (ii), and (iii) in the central strand are then heated first, at approximately 1800 s, followed by those in the two other strands at 2500 s, with the final field line being heated at 2200 s. Since field line (vi) is outside the strands, this demonstrates that the avalanche extends beyond the driven region.

The heating is bursty, both spatially and temporally, and has no obvious preferred location. However, as a result of strong thermal conduction, the temperature and density are spatially smoothed out along the field line, so that the asymmetries in the heating are not reflected in the temperature profiles. All field lines have sustained temperatures (1–2 MK) and densities ($5 \times 10^{14}$–$10^{15}$ m$^{-3}$), with apex densities somewhat lower, although there is considerable structure in time, especially of the temperature, which varies in the range 0.5–2 MK. These values are characteristic of emission from the quiet corona (e.g. Dere et al. 2007; Dere 2020). Also to be noted are the upwards and downwards motion of the TR in response to the bursts of heating, best seen in the temperature contour plots. Thus, these results demonstrate the proof of our conjecture that using the output of a 3D model can give coronal properties when the heating function is implemented in a 1D model. As we demonstrate in Appendix A, this is independent of the initial temperature and density: in particular, the temperature and density used in the MHD model cannot be sustained, as we discuss shortly.

Fig. 3 shows that, despite considerable spikiness in the heating function, the temperature and density do not fall below coronal values, indicating that the bursty heating is somewhere between 'steady' and 'intermediate' (Cargill, Warren & Bradshaw 2015); in other words, the cadence of the heating is shorter than, or of the order of, a typical cooling time (Cargill 2014). The levels of fluctuations are greater in temperature than in density, consistent with the intermediate-frequency nanoflare simulations of Cargill et al. (2015) and Johnston et al. (2017b).

Evidence for this also comes from the emission measure distribution as a function of temperature, EM($T$), where:

$$\mathrm{EM}\,(T) = \int n_e^2 \,\mathrm{d}h, \tag{3}$$

with d$h$ along the line of sight. We follow the approach of Klimchuk et al. (2008) and Cargill (2014), which assumes that a single time series from one field line corresponds to a snapshot from many field lines. Using the output from field line (ii), the EM distribution is peaked around 1.2 MK, with a value around $7 \times 10^{35}$ m$^{-5}$ for a 9 Mm line of sight. The emission measure profile shows tails on both sides, extending up to 3 MK and down to 0.5 MK, as is expected from intermediate-frequency heating. The green curves in Fig. 3 show the temperature and density obtained by inserting the averaged heating into simple, 1D, static scaling laws for loops. We use the formulation of Martens (2010), as presented in section 3.1 of that paper. These imply:

$$T \propto Q^{\frac{2}{7}} L^{\frac{4}{7}} \tag{4a}$$

$$n \propto Q^{\frac{1}{2}} T^{\frac{1}{4}}, \tag{4b}$$

with the scaling constants as given by Martens (2010). Clearly, the bursty heating introduces rapid fluctuations of the temperature and density, but the trends of the scaling law solutions show good agreement with the full model. This suggests that the 1D code, with the implanted TRAC method, is modelling the mass exchange between chromosphere and corona correctly. However, it should be noted that use of scaling laws alone as a model for plasma evolution with this heating function would lead to an excess of both hotter and cooler plasma.

The values of the temperature and density depend on the driving velocities in the MHD simulations. We have performed simulations with twice the present driving speed, as shown in Reid et al. (2020). Using the derived heating in the HD model, temperatures of the order of 2 MK and densities closer to $10^{15}$ m$^{-3}$ are obtained, approaching those more associated with active regions. However, this faster driving exacerbates the problems mentioned in footnote 3.

Inspection of the velocity contour plots shows considerable asymmetry in response to the heating. For an impulsive heating event, one would expect to see an evaporation/draining cycle, first with an upflow, then with a downflow (e.g. Klimchuk et al. 2008; Reale 2014; Cargill et al. 2015), so that the colours in Fig. 4 will alternate as a function of time at any given location. The lowest panel of Fig. 3 indicates that the magnitude of the flows is of the order of 20 km s$^{-1}$. Considering field line (ii) first, at approximately $t = 2000$ and $t = 6000$ s, the heating is concentrated to the left (Fig. 2b) and this leads first to an upflow, which extends over almost the entire loop, and then, after the peak density is reached, the loop drains almost entirely to the left-hand footpoint. On the other hand, at approximately $t = 11500$ s, heating towards the right-hand footpoint leads to anti-parallel upflows, then to parallel downflows. For field line (v), these effects are also clear, witnessed by the heating around 8 Mm at $t = 5500$ s and associated motions.

Examining Fig. 4 shows very few cases that are close to being symmetric: around $t = 6500$ and $t = 8700$ s for field line (ii) are

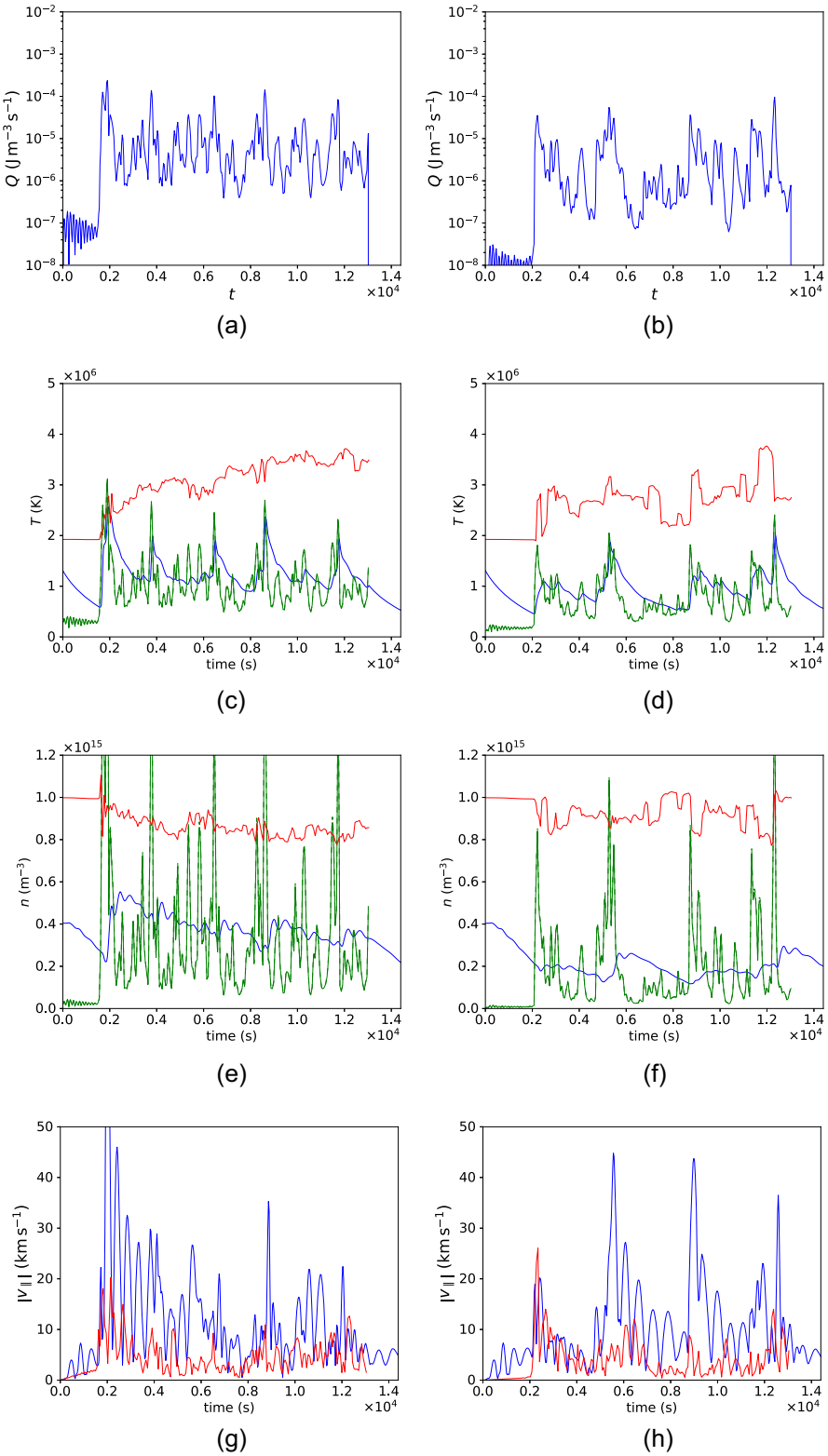


**Figure 3.** Averages of heating (top row), temperature ($T$, second row), number density ($n$, third row), and parallel velocity ($|v_{\parallel}|$, bottom row), for field lines (ii) (left column) and (v) (right). For the temperature, density, and velocity, coronal averages are taken over the half of the field line lying around the loop apex, and shown in blue. For velocity, the absolute value of field-aligned velocity is averaged. Red curves represent the results from the 3D model, green values obtained by inserting the average heating into the scaling laws of Martens (2010).

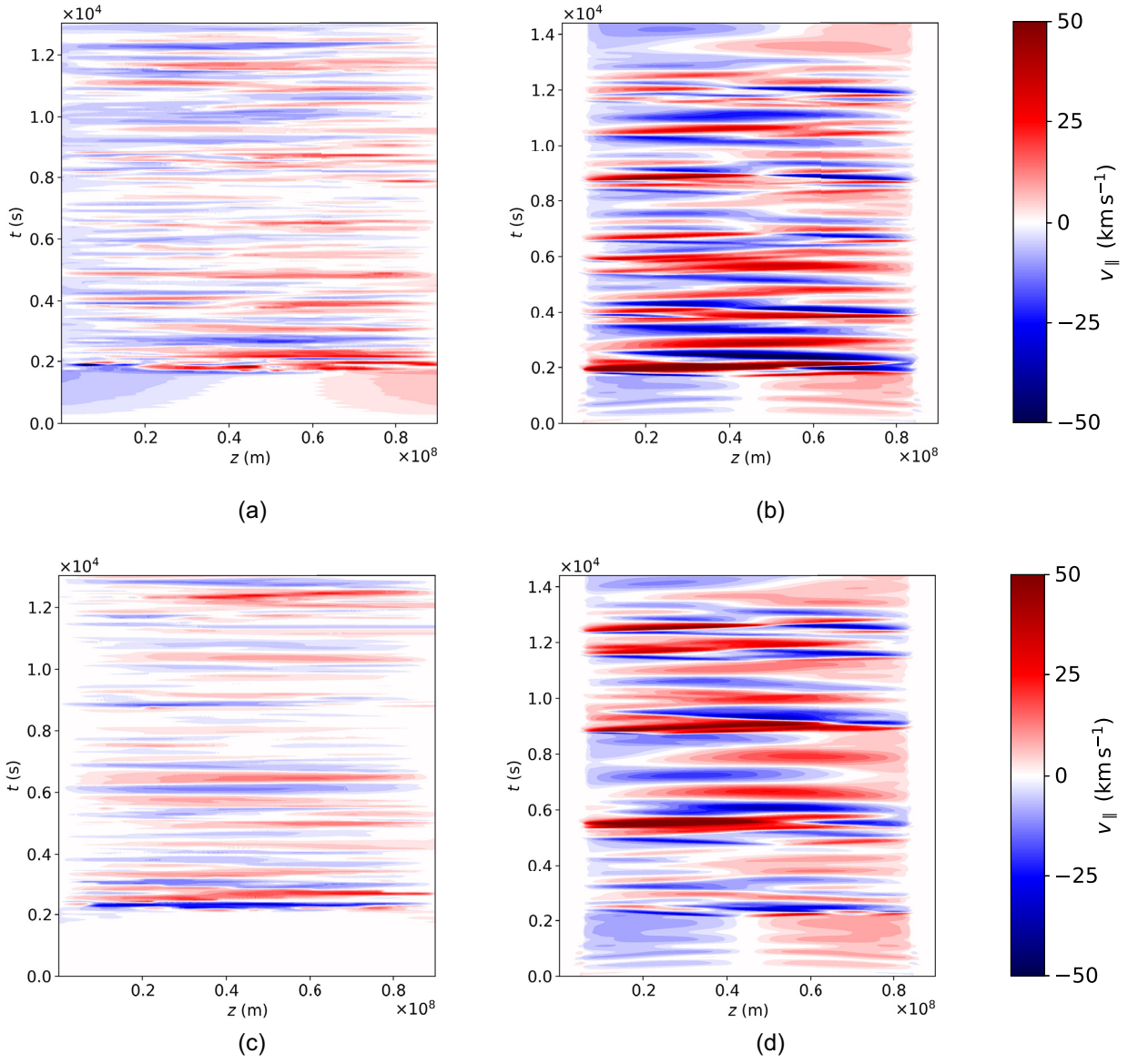


**Figure 4.** Contour plots in the same format as Fig. 2 of the flows along magnetic field line (ii) in the upper row and field line (v) in the lower row. The left and right columns show the results from the 3D MHD and 1D models, respectively. Red and blue colours indicate, respectively, flows parallel and anti-parallel to the magnetic field.

examples. At $t = 6500$ s, the heating burst is at the centre, and we find first an upflow from each footpoint, then a downflow to each. What this demonstrates is that, for a heating function determined from a sufficiently sophisticated MHD model, there is little symmetry in the resulting dynamics: thermal conduction spreads heat efficiently to make the temperature *look* semi-symmetric, but this is not true for the plasma motions. The assumption of symmetry about the loop apex made by many authors would not appear to be a useful tool in interpreting fully 3D results.

### 3.1 Differences between plasma evolution in three dimensions and in one dimension

We now compare the spatially averaged density and temperature obtained in the 3D MHD and 1D models. The red curves in the Fig. 3 show plasma properties obtained in the 3D MHD model along field lines (ii) and (v), under the influence of the heating functions. In the 3D model, the temperature continually increases, since there are no losses from the system, such as conduction and radiation. The density undergoes smaller fluctuations. While the boundary conditions ensure that the total mass in the simulation box is conserved, the local density does show changes. In part, the decrease in the coronal density is a reflection of the averaging over the coronal portion of the field lines. However, another effect is that plasma heating near the apex leads to field-aligned pressure gradients, which push plasma out of the corona, towards the footpoints.

The temperature and density given by the 1D model are both lower than those in the 3D model, so that the 3D temperature and density are inconsistent with the actual temperature and density given by the heating function. In principle, it should be possible to adjust the initial 3D temperature and density such that the heating gives similar values in 3D and 1D, but this is likely to be a painstakingly

iterative process, expensive on computational time. Thus, after the initial instability, the 3D temperature and density no longer reflect the properties of the system and information about the initial temperature and density is lost, a conclusion that applies to a range of initial states (see Appendix A). (A complication is that, as the density changes, and, to a lesser extent, so too does the temperature, the feedback of the plasma evolution on the MHD results will also change. We return to this point in the Section 4.)

While the changes in temperature (such as the sharp increases) in the 1D model are generally also reflected in 3D, there are interesting exceptions, where the 1D average temperature increases in response to heating, while the 3D average temperature falls. One good example arises at 12 500 s for field line (v). Inspection of the 3D results show that, while the heating does locally increase the temperature, the averaging over 50 per cent of the loop leads to the decrease in the average temperature, because the associated reconnection places a volume of unheated plasma on this field line. In the real Sun, this would not be the case, since thermal conduction would very rapidly spread the hot plasma onto the cool, newly reconnected field line.

Field-aligned mass motions also show significant differences between the models. The lowest panels of Fig. 3 show the field-aligned flows associated with the 1D (blue) and 3D (red) models, for field lines (ii) and (v). The left column of Fig. 4 shows the field-aligned flows from the 3D model for the same field lines. The field-aligned flows associated with the 3D model are slow, typically $10\,\mathrm{km\,s^{-1}}$, as shown previously (Reid et al. 2020, in fig. 5). Also, their time histories, shown in Fig. 4, bear little resemblance to the 1D results. On the other hand, in the 1D evolution, faster velocities arise, perhaps by a factor of 2 to 3 in magnitude. The flows have different origins in each model. In 3D, these are localized plasma responses along the field line to the heating. While this will also be present in the 1D results, the dominant motion in them is due to the evaporation/draining cycle, as shown in Fig. 4(b) and discussed earlier. This physics is not present in the 3D model.

Looking again at fig. 5 of Reid et al. (2020), we see that the 1D parallel flows calculated here are of the order of the 3D perpendicular flows (i.e. the reconnection jets). Thus, identifying this key signature of reconnection from observations will be made difficult by the field-aligned flows within a field of view. While, in an idealized geometry, the orientation of the loop might distinguish between field-aligned and perpendicular flows, the reality of coronal energy release, as seen in this avalanche model, would make such a distinction fortuitous. However, a modern EUV spectrometer may be able to disentangle the possibly different temperatures of the jets and evaporative flows.

## 4 DISCUSSION

We have demonstrated how the output of a fully 3D MHD simulation of a coronal avalanche can be used to perform a series of field-aligned simulations, consisting of individual field lines. This hydrodynamic model involves a solution of the full energy equation in the corona and transition region, and permits a study of loop filling/draining in response to the heating. The use of a new method, TRAC, enables fast computational times, although it is not essential for the implementation of our approach. For the avalanche considered, there are differences in the evolution of coronal density and temperature along the field lines, but, at least in these instances, these are not likely to be great enough to influence the full MHD evolution. The 1D model does permit field-aligned mass motions different from those present in 3D and their magnitude may pose difficulties in identifying reconnection jets in observations.

The advantages of the proposed approach at this time are multiple, as can be seen by considering the accounting in the present set of simulations. A large, fully 3D, compressible MHD model, such as that used here, takes many days to run. With the *Lare1d* code and TRAC, a model of a single field line runs in under ten minutes. If one wished to model $256^2$ field lines, then a massively parallel approach would give a run-time of one to two days. This would be faster with an adaptive grid, such as in the codes HYDRAD, Argos, or PLUTO (q.v., respectively, Antiochos et al. 1999; Bradshaw & Mason 2003; Mignone et al. 2007), so long as the TRAC method is implemented. This opens up the option of an exploration of parameter space in the solution of the energy equation, such as different radiative loss functions, models of thermal conduction, or non-equilibrium ionization effects, run with the same 3D output. A zero-dimensional code, such as EBTEL (Klimchuk et al. 2008; Cargill, Bradshaw & Klimchuk 2012a, b), would be even faster. This approach has been proposed by Knizhnik et al. (2020); however, rather than take the exact heating function from their MHD code, those authors use the distribution of heating events, modified to ensure agreement with observations of core loops in active regions, thus sacrificing spatial information.

In the long run, it may be expected that fully 3D MHD codes able to handle energy transport correctly can be developed, especially if the TRAC method is used. However, our proposed approach is still likely to be useful, for several reasons. One, mentioned above, is the ability to perform 1D simulations with different physics for the same 3D run. Secondly, if plasma diagnostics in the lower transition region are required, TRAC cannot be used, since it modifies the atmosphere at temperatures below roughly 20 per cent of the maximum temperature; we previously noted in Johnston et al. (2020) that emission measure profiles are incorrect in that region. In that case, the 3D code would require a high-resolution mesh in that region, with very severe restrictions on the time step and run-time. Finally, while TRAC has been implemented in simple 2D MHD problems (Johnston, Hood, De Moortel, Pagano, and Howson, submitted; Zhou et al. 2021), in complex systems, such as in the avalanche model discussed here, it is unclear how well TRAC can be implemented; once again, ours may be a simpler, but more pragmatic, way of modelling the plasma response.

An important approximation is the neglect of feedback of the plasma on the magnetic field in the 1D model. In the 3D model, this can occur through changes in the pressure, via the term $\nabla P$ in the momentum equation, and through the density, which will influence the Alfvén speed, which scales as $v_A \sim 1/\sqrt{n}$. For the present example, as long as $\beta \ll 1$, the pressure changes will have little effect. An enhanced density decreases $v_A$ and will 'mass-load' the magnetic field, inhibiting the motion of field lines around a reconnection site; the opposite arises for the case of reduced density. We note that, in our case, the difference in the density between the 1D and 3D models is, at most, a factor of 2, so the effect should be modest.

The feedback of the density evolution on 3D MHD reconnection has not been studied in isolation since, as we noted earlier, 3D models either have difficulty in treating thermal evolution well, or are so complex that such an effect cannot be isolated. In this case, the change in the density is modest, however, this effect may be more important in 'low-frequency' nanoflares, whereby individual field lines become evacuated (Cargill 1994).

A further omission from the hydrodynamic model is magnetic reconnection among 3D field lines, in which the identity of field lines is not preserved. Field line (ii), as defined by its initial footpoint position at $x \approx 0.38$, $y = 0$, $z = -L$, is a good example. Early in the

MHD simulation, this field line maintains connectivity to the same plasma elements, on each boundary and along its length. However, as the avalanche proceeds, field line (ii) reconnects somewhere with another field line, which has a different plasma, has a different history of heating, and is associated with a different footpoint on $z = L$. While the routine for tracking field lines in the 3D model calculates the heating along the new, reconnected field line, the 1D model does not allow for reconnection, and so the heating is input into its previous plasma distribution; temperature and density in the 1D model are not adjusted. Although thermal conduction would efficiently remove any differences, the different plasma could, in theory, respond differently to the new heating profile. In this case, in which all field lines sustain a typically coronal temperature, this presents a minor problem. On the other hand, in the low-frequency nanoflare scenario, where field lines cool and are evacuated prior to re-heating, the problem may be more significant, and will especially affect the predicted emission from hot, tenuous plasma, the properties of which are sensitive to the pre-heating temperature and density conditions (e.g. Barnes, Cargill & Bradshaw 2016; Barnes 2019). In such a case, a much more complex algorithm for field lines would be required, involving tracking their properties over the entire grid.

## ACKNOWLEDGEMENTS

JR acknowledges the support of the Carnegie Trust for the Universities of Scotland.

JR and AWH acknowledge the financial support of the Science and Technology Facilities Council (STFC) through the Consolidated grant, ST/S000402/1, to the University of St Andrews.

AWH acknowledges support from the European Research Council (ERC) through Synergy grant 'The Whole Sun' (810218).

CDJ acknowledges funding from the ERC under grant agreement No. 647214.

The authors are grateful to the anonymous referee for instructive and useful comments.

In addition, the authors are grateful to Professors Ineke De Moortel and Clare Parnell for fruitful discussion and support in preparing the manuscript.

Furthermore, the authors are further grateful to Dr Benjamin M. Williams for the code used for all tracing of field lines for the purposes of this paper; the code uses an Runge–Kutta–Fehlberg fourth/fifth-order scheme, details of which are presented by Williams (2018).

This work used the DiRAC@Durham facility, managed by the Institute for Computational Cosmology (ICC), and the Cambridge Service for Data Driven Discovery (CSD3), part of which is operated by the University of Cambridge Research Computing, on behalf of the STFC Distributed Research utilizing Advanced Computing (DiRAC) HPC Facility (https://dirac.ac.uk/). The DiRAC@Durham equipment was funded by BEIS capital funding via STFC capital grants ST/P002293/1 and ST/R002371/1; Durham University; STFC operations grant ST/R000832/1; BIS National E-infrastructure capital grant ST/K00042X/1; STFC capital grant ST/K00087X/1; and DiRAC Operations grant ST/K003267/1. The DiRAC component of CSD3 was funded by BEIS capital funding via STFC capital grants ST/P002307/1 and ST/R002452/1 and STFC operations grant ST/R00689X/1. DiRAC is part of the National e-Infrastructure.

This work used the NUMPY (Oliphant 2006) and MATPLOTLIB (Hunter 2007) PYTHON packages.

## DATA AVAILABILITY

The data underlying this article will be shared on reasonable request to the corresponding author.

## REFERENCES

Antiochos S. K., MacNeice P. J., Spicer D. S., Klimchuk J. A., 1999, ApJ, 512, 985
Arber T., 2018, LareXd User Guide. University of Warwick, Coventry
Arber T. D., Longbottom A. W., Gerrard C. L., Milne A. M., 2001, J. Comput. Phys., 171, 151
Barnes Will Thomas, 2019, PhD thesis, Rice University
Barnes W. T., Cargill P. J., Bradshaw S. J., 2016, ApJ, 829, 31
Bingert S., Peter H., 2011, A&A, 530, A112
Botha G. J. J., Arber T. D., Hood A. W., 2011, A&A, 525, A96
Bowness R., Hood A. W., Parnell C. E., 2013, A&A, 560, A89
Bradshaw S. J., Cargill P. J., 2013, ApJ, 770, 12
Bradshaw S. J., Mason H. E., 2003, A&A, 407, 1127
Cargill P. J., 1994, ApJ, 422, 381
Cargill P. J., 2014, ApJ, 784, 49
Cargill P. J., Bradshaw S. J., Klimchuk J. A., 2012a, ApJ, 752, 161
Cargill P. J., Bradshaw S. J., Klimchuk J. A., 2012b, ApJ, 758, 5
Cargill P. J., Warren H. P., Bradshaw S. J., 2015, Phil. Trans. Roy. Soc. A, 373, 20140260
Dahlburg R. B., Einaudi G., Taylor B. D., Ugarte-Urra I., Warren H. P., Rappazzo A. F., Velli M., 2016, ApJ, 817, 47
Dahlburg R. B., Einaudi G., Ugarte-Urra I., Rappazzo A. F., Velli M., 2018, ApJ, 868, 116
Dere K. P., 2020, MNRAS, 496, 2334
Dere K. P., Doschek G. A., Mariska J. T., Hansteen V. H., Harra L. K., Matsuzaki K., Thomas R. J., 2007, PASJ, 59, S721
Goldstraw E. E., Hood A. W., Browning P. K., Cargill P. J., 2018, A&A, 610, A48
Gudiksen B. V., Carlsson M., Hansteen V. H., Hayek W., Leenaarts J., Martínez-Sykora J., 2011, A&A, 531, A154
Hunter J. D., 2007, Comput. Sci. Eng., 9, 90
Johnston Craig David, 2018, PhD thesis, University of St Andrews, St Andrews
Johnston C. D., Bradshaw S. J., 2019, ApJ, 873, L22
Johnston C. D., Hood A. W., Cargill P. J., De Moortel I., 2017a, A&A, 597, A81
Johnston C. D., Hood A. W., Cargill P. J., De Moortel I., 2017b, A&A, 605, A8
Johnston C. D., Cargill P. J., Antolin P., Hood A. W., De Moortel I., Bradshaw S. J., 2019, A&A, 625, A149
Johnston C. D., Cargill P. J., Hood A. W., De Moortel I., Bradshaw S. J., Vaseekar A. C., 2020, A&A, 635, A168
Klimchuk J. A., 2015, Phil. Trans. Roy. Soc. A, 373, 20140256
Klimchuk J. A., Patsourakos S., Cargill P. J., 2008, ApJ, 682, 1351
Knizhnik K. J., Barnes W. T., Reep J. W., Uritsky V. M., 2020, ApJ, 899, 156
Lionello R., Linker J. A., Mikic Z., 2009, ApJ, 690, 902
Martens P. C. H., 2010, ApJ, 714, 1290
Mignone A., Bodo G., Massaglia S., Matsakos T., Tesileanu O., Zanni C., Ferrari A., 2007, ApJS, 170, 228
Mikić Z., Lionello R., Mok Y., Linker J. A., Winebarger A. R., 2013, ApJ, 773, 94
Oliphant T. E., 2006, A Guide to NumPy. Trelgol Publishing, USA
Orlando S., Bocchino F., Reale F., Peres G., Pagano P., 2008, ApJ, 678, 274
Pontin D. I., Hornig G., 2020, Liv. Rev. Sol. Phys., 17, 5
Reale F., 2014, Liv. Rev. Sol. Phys., 11, 4
Reid Jack, 2020, PhD thesis, Univ. St Andrews, St Andrews
Reid J., Hood A. W., Parnell C. E., Browning P. K., Cargill P. J., 2018, A&A, 615, A84
Reid J., Cargill P. J., Hood A. W., Parnell C. E., Arber T. D., 2020, A&A, 633, A158
van Ballejooijen A. A., Asgari-Targhi M., Cranmer S. R., DeLuca E. E., 2011, ApJ, 736, 3

Van Doorsselaere T., Antolin P., Yuan D., Reznikova V., Magyar N., 2016, Front. Astron. Space Sci., 3, 4
Williams Benjamin Matthew, 2018, PhD thesis, Univ. St Andrews, St Andrews
Zhou Y.-H., Ruan W.-Z., Xia C., Keppens R., 2021, A&A, 648, A29

## APPENDIX A: SENSITIVITY TO INITIAL CONDITIONS

The field-aligned simulations in the main body of this paper feature initial conditions with typical coronal temperature and density, as would be sustained in equilibrium by a background heating term, as mentioned in Section 2.2. It is of interest to determine whether coronal conditions can be created from an initially chromospheric state, and to compare with evolution from the hot, dense initial conditions of the MHD simulation.

In Fig. A1, the evolutions of coronal temperature and density are shown in blue, starting from the initial conditions used throughout the paper, namely a temperature and density of 1.2 MK and $4 \times 10^{14}\,\mathrm{m}^{-3}$. The red curves reflect behaviour starting from a chromospheric initial temperature ($T = 10^4$ K) and a corresponding number density, subject to a minimum $n = 10^{13}\,\mathrm{m}^{-3}$, representing an 'evacuated' loop. Finally, the green curves show evolution from a stratified equilibrium, such that the initial coronal averages of temperature and density approximately match those prevailing in the original MHD simulation. Clearly, the influence of the initial state is rapidly lost, and thus the state of the plasma on the field line is determined chiefly by the recent history of its heating. Other initial states (such as the second case shown here, without imposing a minimum density) have been considered similarly; all cases return a qualitatively similar effect.

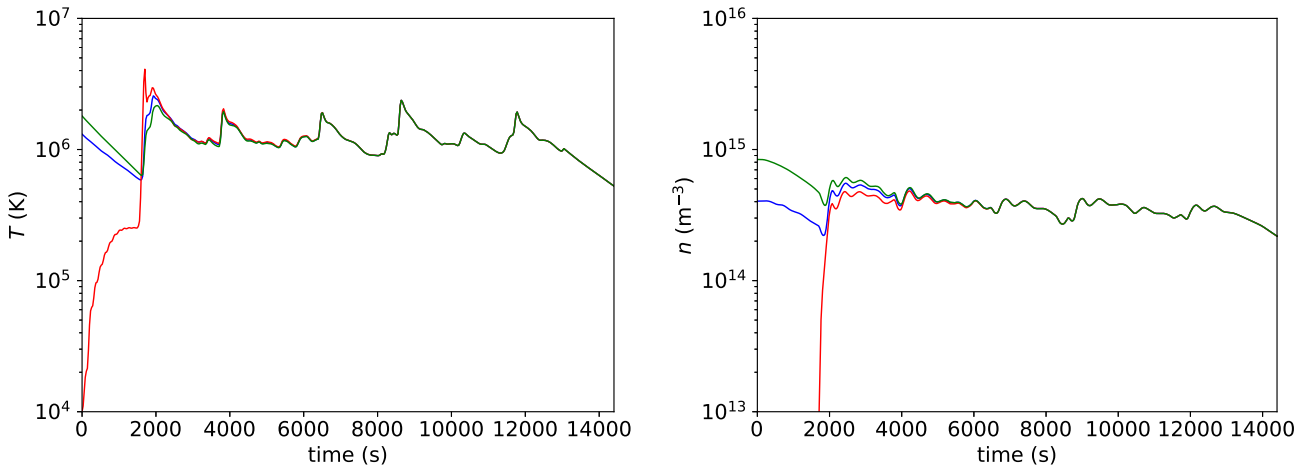


(a) Temperature. (b) Number density.

**Figure A1.** Comparison of the evolution of coronal (a) temperature and (b) density for the initial conditions used throughout the paper (blue), for an initially chromospheric temperature with correspondingly lower number density (red), and for a stratified equilibrium created such that the coronal conditions very closely approximate the initial conditions in the MHD simulation (green). Field line (ii) from the sample is used. For the purposes of this plot, 'coronal average' is defined as for Fig. 3.

This paper has been typeset from a TEX/LATEX file prepared by the author.